PHYSICAL REVIEW A VOLUME 44, NUMBER 11 1 DECEMBER 1991

Electron-ion collisions by the R-matrix method with multichannel quantum-defect theory

Xiaochuan Pan
Department of Physics, University of Chicago, Chicago, Illinois 60637
and The James Franck Institute, University of Chicago, Chicago, Illinois 60637
(Received 3 June 1991)

Collisions are treated by a method that has been very successful in calculating atomic spectra. Results of electron collisions with Be^+, Mg^+, and Ca^+ are presented, showing extensive series of double excitation resonances of the collision complex. Convergence of the results to the limit of peripheral collisions, where the Born approximation holds, is displayed. Cross sections of optically allowed and forbidden excitations are evaluated, including cascade effects and distributions in the scattering angle. The polarization of emissions from the excited target is calculated successfully.

PACS number(s): 34.10.+x, 34.50.Fa, 34.90.+q

I. INTRODUCTION

Collisions of a projectile (electron, proton, etc.) with a target (ion, atom, molecule, etc) may have an impact parameter comparable to, or much larger than, the target size. These alternative physical circumstances may be explored by different treatments. In peripheral collisions (with large impact parameters), the projectile fails to penetrate the target, thus remaining distinct from it. The absence of correlations between projectile and target affords simpler treatments, such as the Born approximation. A more elaborate treatment is required when projectile and target intermingle in a *single collision complex*. The main contribution of this paper consists of developing and applying a treatment of the collision complex. Earlier papers have indicated how to combine separate treatments [1] of the complex and of peripheral collisions and also how to sort out corresponding experimental data [2]. The treatment of peripheral collisions in the Coulomb-Born approximation has required a lesser effort.

Our treatment of the collision complex formed at short impact parameters demonstrates its convergence to the results of a simpler Born approximation for increasing values of the orbital quantum number [3]. It deals specifically with electron-ion collisions, but its method can be extended to collisions of atoms, molecules, and particles with a similar transition from collision complex to peripheral processes.

The present treatment of a collision complex combines the eigenchannel R-matrix approach [4] with the multichannel quantum-defect theory (MQDT) [5,6] in a manner that has proved very successful in describing optical spectra of atoms to spectroscopic accuracy [7–10], but has not been utilized previously for collisions. This extended application requires separate calculations for a larger set of orbital momenta and inclusion of a larger set of channels for each orbital momentum. We have now applied this approach to low-energy ($\lesssim 13$ eV) electron-ion collisions, where strong correlations between projectile and target electrons occur in a transient collision complex. The incident electron and the target electrons to be excited are treated on equal footing, being subjected to the same potential from the target core.

Electron collisions with monovalent ions (Be^+, Mg^+, Ca^+) were chosen for this study as counterparts to the two-electron spectroscopy of alkaline-earth elements [7,8]. Extension to multielectron open shells may proceed in the future together with the spectroscopy of neutral atoms. Extension of electron–neutral-atom collisions will similarly fit into MQDT procedures, as well be discussed in Sec. IV.

This approach affords a systematic and comprehensive treatment of the prominent and complicated series of double excitation states of the collision complex. It yields not only cross-section information but also a rich variety of valuable and detailed structure information on the collision complex as well as on other processes such as dielectric recombination. Fragmentary evidence of double-excitation series had emerged in earlier experiments [11–14] as well as in theoretical calculations by close coupling [15,16], the diagonalization method [17], and other familiar procedures [18,19], but MQDT will prove particularly apt to bring out its extensive details. A comparison of the performance of our approach with that of close coupling and other advanced procedure will be presented in Sec. IV. This paper presents studies of electron-impact excitation of Be^+, Mg^+, and Ca^+, with particular emphasis on the first optical resonance transition in the target ions, namely $Be^+(2s \rightarrow 2p)$, $Mg^+(3s \rightarrow 3p)$, and $Ca^+(4s \rightarrow 4p)$.

Evaluation of a collision cross section requires, in principle, an infinite number of partial waves. However, no elaborate treatment is needed for the contributions from high partial waves (here $L > 7$) for which the projectile remains peripheral, failing to traverse the target and hence to correlate with target electrons. These contributions may, however, be provided adequately by a Born approximation. An important aspect of this work displays quantitatively the convergence of the results of the elaborate treatment to those of the Born approximation. The Coulomb-Born approximation [20] is actually adopted in this work to evaluate the high partial waves because the projectile electron is always under the influence of the Coulomb field from the target ion. This convergence has been found to hold within a few percent in $L>7$ for $e+\mathrm{Be}^+$, Mg^+, and Ca^+ at energies $\lesssim 13$ eV.

The MQDT treatment of R matrices for each set $(LS\pi)$ provides, in principle, the elastic and inelastic cross sections for *all the transitions* between target states accessible in the energy range studied. It includes the orientation and alignment parameters observed through the polarization of optical emissions [21,22]. Experimental evidence consists mainly of photoemission cross sections [13,14,23], which include *cascade* contributions, and polarizations. These contributions are readily sorted out from our calculations and unraveled from experiments.

Section II reviews the theory and the calculation arrangements for the noniterative eigenchannel R-matrix approach with MQDT. The original R-matrix theory of Wigner and Eisenbud [24] has been widely used to deal with strong electron correlations in atomic and molecular physics [18,19]. The eigenchannel R-matrix method is an alternative approach introduced in atomic theory by Fano and Lee [4]. A variational noniterative reformulation by Greene of the eigenchannel R-matrix method has greatly improved its efficiency [25,26]. When combined with analytical MQDT, it provides a successful description of the complicated atomic spectrum observed, demonstrated through numerous applications to atomic and negative ions in the past few years [7–10].

In Sec. III, extensive results are presented and compared with the existing experimental data [11–14,23] as well as with other theoretical results [15–19]. Notable discrepancies exist between experimental data and some earlier theoretical predictions. For instance, there is a long-standing $\sim 15\%$ discrepancy of the experimental cross section in $e+\mathrm{Be}^+(2s\rightarrow 2p)$ [23] as compared to the theoretical results (even with the most advanced close-coupling calculation by Mitroy and Norcross [27]). Our treatment improves the results and shows the series of double excitation resonance that are not resolved in the experiment. It proves that correct evaluation of contributions from low partial waves $(L\leq 7)$ are essential for obtaining good cross-section results. These contributions make up more than 90% and $\sim 80\%$ of the total cross sections for low and high portions of the energy range studied.

The convergence of the results by the R matrix with MQDT to those by the Coulomb-Born approximation is displayed quantitatively. Excitation cross sections to higher levels by electron impact are also sorted out systematically and their contributions to the observed photoemission cross section by cascade are evaluated. Angular distributions of the scattered electrons are presented here, especially near the double excitation energies. Thus far no such experimental data are available, but our results may provide useful information for future measurements. Polarizations of the excited target decays are evaluated and agree well with experiments [13,14,23].

Section IV contains discussions of the comparisons of our calculations with other advanced procedures (distorted wave, close coupling, diagonalization method, etc.), focusing on analysis of the physical reasons for their differences. Further applications accessible within the frame of the present work are noted, outlining the extension of the current approach to other processes. Limitations of this treatment are also commented upon.

II. THEORY

A. R-matrix calculation and eigenchannels

The R-matrix method enables one to evaluate observable effects of complicated short-range correlations among the electrons within a finite space volume V without analyzing their origin. Outside the surface S of this reaction volume V, correlations are usually disregarded. A noniterative formulation of the eigenchannel R-matrix method and of its implications for atomic spectra accounting analytically for phenomena external to V has been discussed in detail by Greene *et al.* [7–10]. A later "streamlined" version [28] of this formulation is utilized in the present study.

In this work, where electron collisions with alkaline-earth-metal ions are studied, the Hamiltonian for the collision system is represented adequately below the two-electron ionization threshold, in the a.u. form [29],

$$H=h(\mathbf{r}_1)+h(\mathbf{r}_2)+\frac{1}{r_{12}}\ . \tag{1}$$

In Eq. (1), the incident electron and the valence electron of the target are treated equivalently. The effective one-electron Hamiltonian $h(\mathbf{r})$ consists of the electron kinetic energy $-\frac{1}{2}\nabla^2$ and of a radial l-dependent potential $v_l(r)$. This $v_l(r)$ depicts the net screened nuclear Hartree-Slater (HS) potential experienced by a valence electron of the target, complemented by an empirical core-polarization term [30]:

$$v_l(r)=v_l^{\mathrm{HS}}(r)-\frac{\alpha_l}{2r^4}\left(1-e^{-(r/r_{\mathrm{cl}})^6}\right)\ . \tag{2}$$

The core electrons are assumed to be frozen to the extent that they determine $v_l(r)$ correctly. The screening term $v_l^{\mathrm{HS}}(r)$ in Eq. (2) is evaluated by a standard Hartree-Slater procedure. The l-dependent cutoff radius r_{cl} is tuned to obtain optimum agreement with the known experimental energy levels of each target ion (Be^+, Mg^+, and Ca^+) [31]. For the lowest one or two levels of each l (s, p, d, and f waves), our values do not differ more than 0.01% from the experimental spectrum, rising to a few percent for higher levels.

The radius r_0 of the reaction volume, within which the R-matrix calculation is formulated, is determined by selecting a range of collision energies and the set $\{\epsilon^a\}$ of energy levels of the target ion accessible within that range. The value of r_0 is then set by requiring that an electron in any of these levels has no more than 1% probability of reaching beyond it; this probability will be disregarded in the following.

The R-matrix eigenchannel wave functions Ψ_β of the collision system are eigenstates of the Hamiltonian (1) at any desired energy E with a constant normal logarithmic derivative b_β over the surface S enclosing the reaction volume V. A convenient form of the trial wave function Ψ_β consists of a linear combination of specified two-electron wave functions y_k with unknown superposition coefficients C_k^β, $\Psi_\beta = \sum_k C_k^\beta y_k$. The search for a stationary value of b_β leads to a generalized linear eigensystem [29] that determines the coefficients C_k^β and the corresponding eigenvalues b_β,

$$\underline{\Gamma}\,\underline{C} = b\underline{\Lambda}\,\underline{C} \ , \tag{3}$$

where

$$\Gamma_{kk'} = 2\int_V y_k (E - H) y_{k'} dV - \int_S y_k \frac{\partial y_{k'}}{\partial n} dS \tag{4}$$

and

$$\Lambda_{kk'} = \int_S y_k y_{k'} dS \ . \tag{5}$$

Rapid convergence of the calculation hinges on selecting a set of sensible and adequate basis functions y_k. We use antisymmetrized products one-electron orbitals $u_{nl}(r) Y_{lm}(\Omega)$ to construct the two-electron basis functions y_k with definite L, S, and parity π. Eigenstates $(1/r) u_{nl}(r) Y_{lm}(\Omega)$ of the single-electron Hamiltonian $h(\mathbf{r})$ in Eq. (1) have radial orbitals $u_{nl}(r)$ satisfying

$$-\frac{1}{2}\frac{d^2}{dr^2} u_{nl}(r) + \left[\frac{l(l+1)}{2r^2} + v_l(r) - \varepsilon_{nl} \right] u_{nl}(r) = 0 \ . \tag{6}$$

Two types of radial orbitals $u_{nl}^c(r)$ and $u_{nl}^o(r)$ are generated by solving Eq. (6) within the reaction volume and imposing alternative boundary conditions on the reaction surface $r = r_0$. The "closed" type $u_{nl}^c(r)$ vanish at r_0 exactly and the "open" type $u_{nl}^o(r)$ do not. Thus the "closed" type $u_{nl}^c(r)$ are orthonormal over the range $r \le r_0$ but the $u_{nl}^o(r)$ are not. A lower value subset of the eigenvalues ε_{nl} of u_{nl}^c coincides with the set $\{\epsilon^a\}$ of accessible energy levels of the target ion, to within the accuracy of disregarding the leakage beyond r_0 of the set's eigenfunctions.

The antisymmetrized LS-coupled two-electron basis functions y_k are thus expressed in terms of one-electron orbitals by [29]

$$\begin{aligned} y_k(\mathbf{r}_1, \mathbf{r}_2) = \frac{1}{\sqrt{2}} [& \phi_{n_1 l_2 l_2}^{LS}(r_1, \Omega_1, \Omega_2) u_{n_2 l_2}(r_2) \\ & + (-1)^{L+S+1} \phi_{n_1 l_1 l_2}^{LS}(r_2, \Omega_2, \Omega_1) \\ & \times u_{n_2 l_2}(r_1)] \ , \end{aligned} \tag{7}$$

where $k \equiv \{n_1, l_1, n_2, l_2\}$, and

$$\phi_{n_1 l_1 l_2}^{LS}(r_1, \Omega_1, \Omega_2) = u_{n_1 l_1}^c(r_1) Y_{l_1 l_2 LM}(\Omega_1, \Omega_2) \tag{8}$$

vanishes at $r_1 = r_0$.

Each basis function y_k can thus be labeled as $y_{n_1 l_1 n_2 l_2}$, where $n_1 l_1$ pertains to closed orbitals only and $n_2 l_2$ refers to open or closed orbitals. As noted above, the two-electron basis functions y_k will be similarly labeled as y_k^o and y_k^c when they do or do not include open orbitals.

The set of "closed" bases y_k^c, allowing neither electron to reach the reaction surface, spans the reaction volume V, and serves to describe solutions of Eq. (1) that vanish on the reaction surface S. Further adding a small number of "open" y_k^o to the set of y_k^c provides the flexibility to represent any solution Ψ_β, which allows the escape of one electron from the reaction volume with a specific logarithmic derivative on the reaction surface S. Alternative use of the basis sets $\{y_k^c\}$ and $\{y_k^o\}$ affords the expeditious "streamlined" procedure introduced by Greene *et al.* [28].

As mentioned above, the energy range to be treated and the channels retained in the R-matrix calculation dictate the radius r_0 of the reaction volume V. We have utilized the value $r_0 = 31$ a.u., beyond which the wave function is negligible for all (nl) target states accessible in the energy range treated here. For example, in the energy range at which $e + \mathrm{Be}^+$ is studied, $4d\epsilon l$ is the highest accessible channel retained. The value $r_0 = 31$ a.u. is thus roughly the smallest distance beyond which the $4d$ orbital of Be^+ effectively vanishes. Test results with larger r_0 have shown negligible effects on the final cross sections.

This moderately large value of r_0 requires a correspondingly large set of orbitals u_{nl}^c. We have used 12 "closed" type and 2 additional "open" type radial orbitals for each l. Test calculations with larger sets of u_{nl}^c have yielded no appreciable improvement of the final results.

The LS-coupling scheme has been adopted in our R-matrix calculation. The number of channels included in the calculation ranges from 9 to 20 for each set of $(LS\pi)$. For instance, the 13 channels used for the $L = 1$, $S = 1$, and $\pi = -1$ set of $e + \mathrm{Be}^+$ are $\{2s\epsilon p, 2p\epsilon s, 2p\epsilon d, 3s\epsilon p, 3p\epsilon s, 3p\epsilon d, 3d\epsilon p, 3d\epsilon f, 4s\epsilon p, 4p\epsilon s, 4p\epsilon d, 4d\epsilon p, 4d\epsilon f\}$.

B. MQDT parameters

Each eigenchannel wave function Ψ_β of the R matrix is expanded into alternative states Φ_i of the residual ion on the reaction surface S:

$$\Psi_\beta = \sum_i \Phi_i(r_1, r_2) F_{i\beta}(r_0) \ . \tag{9}$$

The Φ_i themselves are expressed in terms of the surface harmonics ϕ of Eq. (8) as

$$\begin{aligned} \Phi_i(r_1, r_2, \Omega_1, \Omega_2) & \\ = \frac{1}{\sqrt{2}} [& \phi_{n_1 l_1 l_2}(r_1, \Omega_1, \Omega_2) \\ & + (-1)^{L+S+1} \phi_{n_1 l_1 l_2}(r_2, \Omega_2, \Omega_1)] \ , \end{aligned} \tag{10}$$

with $i \equiv \{n_1, l_1, l_2\}$.

Outside the reaction volume V the field is mainly Coulombic and the wave function of the escaping electron can be represented [29] as a superposition of regular and irregular energy-normalized Coulomb wave functions f and g by projecting Ψ_β onto the state Φ_i on the reaction surface S:

$$\langle \Phi_i / \Psi_\beta \rangle_S = F_{i\beta}(r_0) = f_i(r_0) I_{i\beta} - g_i(r_0) J_{i\beta} \ , \tag{11}$$

$$-b_\beta \langle \Phi_i | \psi_\beta \rangle_s = F'_{i\beta}(r_0) = f'_i(r_0) I_{i\beta} - g'_i(r_0) J_{i\beta} \ , \tag{12}$$

with i and $\beta=1,2,\ldots,N$. This approach disregards the polarization of the target ion by the projectile at $r>r_0$, which is negligible as compared to the monopole Coulomb interaction but may be important in other circumstances [9]. This polarization can be taken into account, if desired, by replacing the Coulomb wave functions $\{f,g\}$ in Eqs. (11) and (12) with solutions of the combined Coulomb and polarization fields [9]. In Eqs. (11) and (12), N is the number of channels retained in the calculation and Φ_i includes both the spin and orbital couplings of the projectile and the target ions. The angular parts of the left-hand side of Eqs. (11) and (12) have been integrated out analytically. The matrix elements $I_{i\beta}$ and $J_{i\beta}$ are determined by Eqs. (11) and (12). They are, in turn, equivalent to the "short-range" $N\times N$ reaction matrix

$$\underline{K}=\underline{J}\,\underline{I}^{-1} \tag{13}$$

with diagonalized form

$$K_{ij}=\sum_{\alpha} U_{i\alpha}\tan(\pi\mu_\alpha)U_{\alpha j} \ , \tag{14}$$

where μ_α is the quantum defect, $\tan\pi\mu_\alpha$ serves as the eigenvalue, and $U_{i\alpha}$ serves as the eigenvectors of the symmetric $\underline{K}$ matrix. The MQDT parameters $\{\mu_\alpha, U_{i\alpha}\}$ embody all the *relevant dynamical information* generated in the reaction volume. They generally depend smoothly on the energy and serve to predict observables such as the scattering or photoionization cross sections [6–10].

The MQDT subdivides the matrix $\underline{K}$ into block [5] matrices:

$$\underline{K}=\begin{bmatrix}\underline{K}_{oo} & \underline{K}_{oc}\\ \underline{K}_{co} & \underline{K}_{cc}\end{bmatrix} , \tag{15}$$

where $\underline{K}_{oo}(\underline{K}_{cc})$ represents the coupling among the open (closed) channels. These submatrices, are, of course, complemented by open-closed channel interactions, represented by $\underline{K}_{oc}$ and $\underline{K}_{co}$. [A channel i is called "closed" when the projectile energy E lies below the energy level ϵ_i^a, thus sufficing to excite this level *only if* the projectile is temporarily captured in a double excitation state. The channel is "open" when $E>\epsilon_i^a$. The notations (c,o) are standard labels for channels in MQDT, but should not be confused with the same labels when applied to basis orbitals as in Eq. (8) here and as in Ref. [29].]

The physical reactance matrix that determines the scattering observables at $r\to\infty$ is then expressed as

$$\underline{K}^o=\underline{K}_{oo}-\underline{K}_{oc}[\tan(\pi\bar{\nu})+\underline{K}_{cc}]^{-1}\underline{K}_{co} \tag{16}$$

by eliminating all of the closed channels as in Sec. 6.4 of Ref. [5]. This elimination is equivalent to summing over contributions from an infinite number of discrete states in the closed channels. The matrix $\underline{K}^o$ has the same $N_o\times N_o$ dimensions as $\underline{K}_{oo}$, where N_o is the number of open channels. The matrix $\bar{\nu}$ in Eq. (16) is diagonal in the base of closed channels with threshold energies $\{\epsilon^a\}$. Each of its elements depends on the energy E according to the Rydberg formula

$$\nu_i=[2(\epsilon_i^a-E)]^{-1/2} \ , \tag{16$'$}$$

causing $\tan\pi\bar{\nu}$ to diverge periodically as E transverses a half-integer value of ν_i.

The leading term of (16), $\underline{K}_{oo}$, includes some influence of the closed channels, but the most visible effects of the closed channels are represented by the second term, specifically by zeros of its denominator. Thereby $\underline{K}^o$ displays sharp resonances at these zeros, unlike the smooth variation of $\underline{K}$. The explicit analytic form of this dependence in (16) is a main contribution of the MQDT treatment.

Each resonance represents the temporary capture of the incident electron, with formation of a doubly excited state of the complex. This state may decay by autoionization, i.e., by escape of the incident electron. On the other hand, it becomes stabilized by *dielectronic recombination* if the escape is preceded by fluorescent transitionn to a lower stable level.

C. Collision formulas

Following standard procedures [5,32], the scattering matrix $\underline{S}$ and the transmission matrix $\underline{T}$ are evaluated in terms of the reactance matrix $\underline{K}^o$ of (16) derived from the MQDT parameters $\{\mu_\alpha, U_{i\alpha}\}$,

$$\underline{S}=\frac{\underline{I}+i\underline{K}^o}{\underline{I}-i\underline{K}^o},\quad \underline{T}=\underline{I}-\underline{S} \ . \tag{17}$$

Equation (17) is a matrix equation, where $\underline{I}$ stands for the identity matrix.

The $\underline{T}$ matrix element $T^{LS\pi}_{n_iL_i\epsilon_il_i,n_fL_f\epsilon_fl_f}$ will be abbreviated as $T^{LS\pi}_{l_il_f}$. Here, l_i and l_f are the initial and final orbital quantum numbers of the projectile, and n_iL_i and n_fL_f are the target quantum numbers before and after the scattering.

A dimensionless collision strength [5], analogous to the optical oscillator strength, is defined for each set $(LS\pi)$ as

$$\Omega^{LS\pi}(i\to f)=\sum_{l_i,l_f}\tfrac{1}{2}(2L+1)(2S+1)|T^{LS\pi}_{l_il_f}|^2 \ , \tag{18}$$

the summation extending over the relevant projectile's orbitals.

The strength $\Omega^{LS\pi}$ not only provides for evaluating cross sections, but also contains extensive structure information about the collision complex, especially on the rich resonance spectra resulting from transient capture of the projectile electron by excited states of the target. Plots of $\Omega^{LS\pi}$, as a function of the incident energy, reveal the successive onsets of series of double excitation resonances converging to the excitation thresholds $\{\epsilon^a\}$ of the target ion. These resonances lie at the zeros of the MQDT determinant [6,23], i.e., at the roots of

$$Det\,|U^c_{i\alpha}(E)\sin\pi[\nu_i(E)+\mu^c_\alpha(E)]|=0 \ . \tag{19}$$

Here, $\tan\pi\mu^c_\alpha$ and $U^C_{i\alpha}$ are the eigenvalues and eigenvectors of the closed portion $\underline{K}_{cc}$ of the $\underline{K}$ matrix (15), and ν_i depends on the threshold energy ϵ_i^{α} of the ith closed channel as in Eq. (16a). Furthermore, the evaluation of an amplitude Z_i in terms of $\{\mu_{\alpha}^{c}, U_{i\alpha}^{c}, \nu_i\}$ as Eq. (7) of Ref. [8] determines the dominant channel to which a resonance belongs.

The total inelastic cross section for a spin unpolarized collision results by averaging the squared scattering amplitude over the initial magnetic states and summing it over the final magnetic states of the orbital and spin momenta and by integrating over scattering angles [33,34]. The cross section is thus expressed in terms of the invariant collision strength $\Omega^{LS\pi}$ by

$$\sigma(i\rightarrow f)=\frac{\pi a_0^2}{k_i^2}\sum_{L,S,\pi}\frac{\Omega^{LS\pi}(i\rightarrow f)}{(2S_i+1)(2L_i+1)} . \tag{20}$$

Here, $\frac{1}{2}k_i^2$ equals the incident energy and (L_iS_i) are the initial orbital and spin momenta of the target. The summation over partial waves L ranges, in principle, to infinity.

The angular distribution of the scattered electron is also calculated from the transition matrix $\underline{T}$ of (17). The differential cross section is obtained, as in (20), by averaging over the initial and summing over the final magnetic numbers [33,34],

$$\begin{aligned}\frac{d\sigma(\theta)}{d\Omega}=&\frac{\pi a_0^2}{k_i^2}\frac{(-1)^{L_i+L_f}}{8(2S_i+1)(2L_i+1)}\\&\times\sum_{L,S,\pi,l_i,l_f}\;\sum_{L',l_i',l_f',\lambda}(-1)^{1/2(l_i-l_i'+l_f'-l_f)}(2S+1)(2L+1)(2L'+1)(2\lambda+1)[l_i][l_f][l_i'][l_f']\\&\times\begin{bmatrix}l_i & l_f & \lambda\\ 0 & 0 & 0\end{bmatrix}\begin{bmatrix}l_i' & l_f' & \lambda\\ 0 & 0 & 0\end{bmatrix}\begin{Bmatrix}l_i & L & L_i\\ L' & l_i' & \lambda\end{Bmatrix}\begin{Bmatrix}l_f & L & L_f\\ L' & l_f' & \lambda\end{Bmatrix}\\&\times\mathrm{Re}(e^{i(\sigma_{l_i}+\sigma_{l_f}-\sigma_{l_i'}-\sigma_{l_f'})}T_{l_il_f}^{LS\pi}T_{l_i'l_f'}^{L'S\pi *})P_{\lambda}(\cos\theta) .\end{aligned} \tag{21}$$

Here, $[l]=(2l+1)^{1/2}$ and the $\{\sigma_l\}$ indicate the phase shifts generated by long-range interactions, Coulombic [32] in this case, the $3j$ and $6j$ coefficients [35] originate from geometric averages, and $P_{\lambda}(\cos\theta)$ indicates the usual Legendre polynomial in the cosine of the scattering angle. The long-range Coulomb phases play an important role in calculating the differential cross section (21) in contrast to the total cross section (20), which results by integrating (21) over the scattering angle θ and considering the symmetries of its coefficients.

The partial cross section for target excitation to a magnetic substate M_{L_f} is [27]

$$\begin{aligned}\sigma_{M_{L_f}}(i\rightarrow f)=&\frac{\pi a_0^2}{k_i^2}\frac{1}{2(2L_i+1)(2S_i+1)}\sum_{S,\pi,l_f,M_{L_i},m_f}(2S+1)\\&\times\left|\sum_{L,l_i}(2L+1)[l_i]i^{l_i}e^{i\sigma_{l_i}}\begin{bmatrix}L_i & l_i & L\\ M_{L_i} & 0 & -M\end{bmatrix}\begin{bmatrix}L_f & l_f & L\\ M_{L_f} & m_f & -M\end{bmatrix}T_{l_il_f}^{LS\pi}\right|^2 .\end{aligned} \tag{22}$$

The Coulomb phase σ_{l_i} is also retained here. These partial wave cross sections serve to evaluate the polarization of photons emitted by the excited target; they will be calculated and compared with experimental results in next section.

D. Coulomb-Born formulas

Evaluating a collision cross section as in Eq. (20) requires, in principle, an infinite number of partial waves. The high partial waves actually contribute substantially to optical excitations of the target ions because of the slow convergence of dipole interactions. In the absence of strong correlations between projectile and target in high partial waves, a simpler treatment in the Born approximation proves adequate, as is documented in the next section.

We utilize here the Coulomb-Born (CB) treatment [36,37], which gives the reactance matrix element

$$K^{(\mathrm{CB})}(n_iL_i\epsilon_il_i,n_fL_f\epsilon_fl_f)=-2\sum_{\lambda}\langle l_fL_fL|P_{\lambda}|l_iL_iL\rangle\mathcal{R}_{\lambda} \tag{23}$$

with an algebraic expression of the angular factor $\langle l_fL_fL|P_{\lambda}|l_iL_iL\rangle$ [38] and radial factor

$$\mathcal{R}_{\lambda}=\int_0^{\infty}f_{\epsilon_fl_f}(r)\Upsilon_{\lambda}(r)f_{\epsilon_il_i}(r)dr , \tag{24}$$

with

$$\Upsilon_\lambda(r)=\frac{1}{r^{\lambda+1}}\int_0^r R_{n_fL_f}(\xi)\xi^\lambda R_{n_iL_i}(\xi)d\xi + r^\lambda\int_r^\infty R_{n_fL_f}(\xi)\xi^{-\lambda-1}R_{n_iL_i}(\xi)d\xi \,. \tag{25}$$

Here, $R_{n_iL_i}$ and $R_{n_fL_f}$ are the radial wave functions of the initial and final states of the target and $f_{\varepsilon l}$ is the regular Coulomb wave function. The dipole term ($\lambda=1$) contributes most to optical excitations.

The transition matrix $\underline{T}$ in the Coulomb-Born approximation is related to $\underline{K}^{(\mathrm{CB})}$ by

$$\underline{T}^{(\mathrm{CB})}=\frac{-2i\underline{K}^{(\mathrm{CB})}}{\underline{I}-i\underline{K}^{(\mathrm{CB})}} \,. \tag{26}$$

Similarly the relevant collision strength and cross section are given by

$$\Omega^{(\mathrm{CB})L\pi}(i\rightarrow f)=\sum_{l_i,l_f}(2L+1)|T_{l_il_f}^{(\mathrm{CB})L\pi}|^2 \tag{27}$$

and

$$\sigma^{(\mathrm{CB})}(i\rightarrow f)=\frac{\pi a_0^2}{k_i^2}\sum_{L,\pi}\frac{\Omega^{(\mathrm{CB})L\pi}(i\rightarrow f)}{(2L_i+1)} \,. \tag{28}$$

III. RESULTS

A. Collision strength and resonances

The collision strength $\Omega^{LS\pi}(i\rightarrow f)$ in Eq. (18) serves mainly to calculate cross sections; however, its study as a function of energy, similar to that of the familiar optical oscillator strength, also reveals structure information,

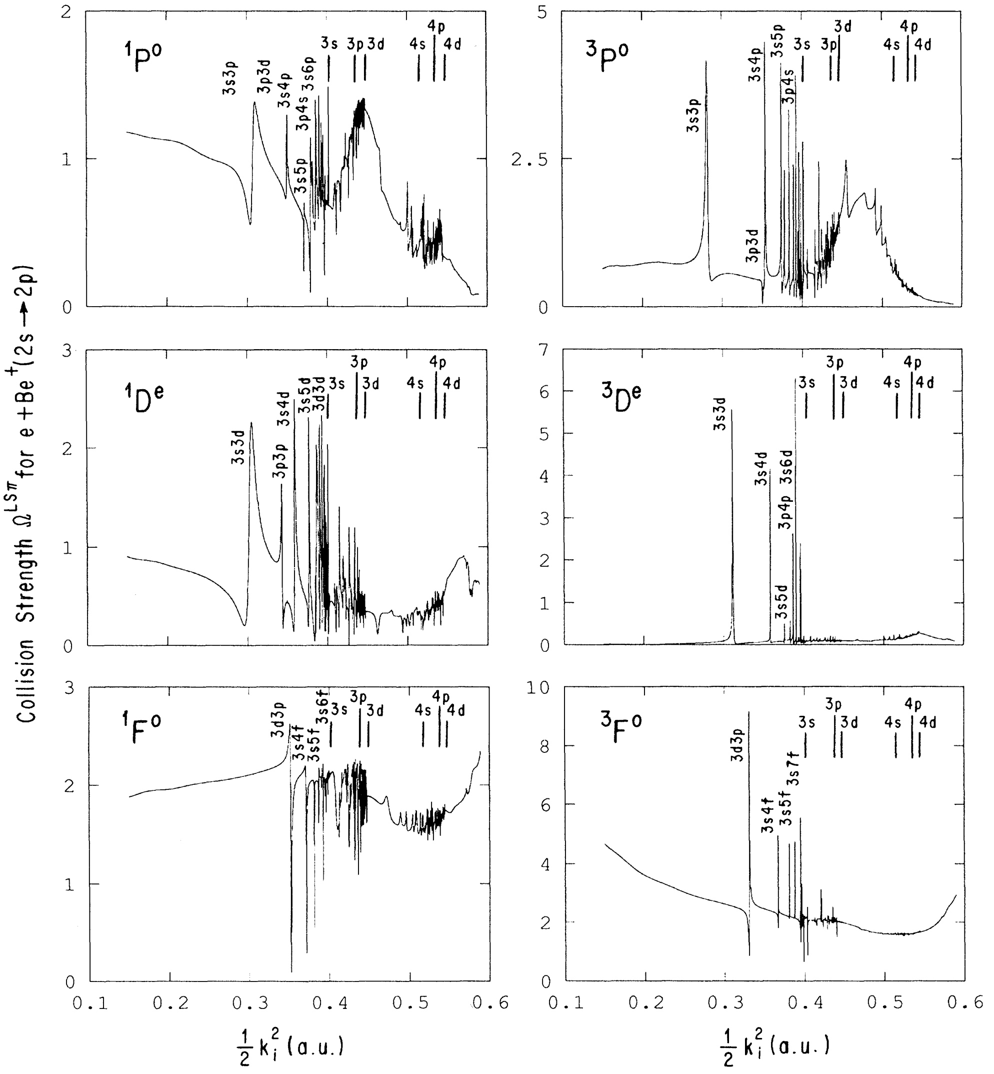

FIG. 1. Dimensionless collision strengths $\Omega^{LS\pi}$ for Be$^+$($2s\rightarrow2p$) and several $LS\pi$. The small vertical lines indicate the excitation thresholds ε_i^a; the abscissas are incident energies $\frac{1}{2}k_i^2$ in a.u. here and in the following figures. Note the different scales in the plots for various $LS\pi$. Some of the narrow resonances in this and the following figures may utilize insufficient energy mesh points to reflect their true heights.

especially the resonance structure of the collision complex. In the present study of electron collisions with Be^+, Mg^+, and Ca^+, these resonances correspond to double excitation states of the alkaline-earth metals Be, Mg, and Ca. The collision strengths $\Omega^{LS\pi}(i \to f)$ for six different $LS\pi$ of $\mathrm{Be}^+(2s \to 2p)$, $\mathrm{Mg}^+(3s \to 2p)$, and $\mathrm{Ca}^+(4s \to 4p)$ are shown in Figs. 1–3. The double excitation resonances form prominent infinite series converging to the excitation thresholds $\{\varepsilon^a\}$ of the target. The energy at which a resonance occurs is determined by a root of the MQDT determinant in Eq. (19). The dominant channel to which a resonance belongs is identified by studying its amplitudes Z_i [6]. Some of the resonance series have been identified in Figs. 1–3; Table I compares our calculated levels with the observed values of $ns\varepsilon p$ resonances in Be and Mg. No experimental data in the present energy range are available for Ca. The classification of these resonances is complicated at high energy, especially near the thresholds, by the numerous channel interactions. The resonances in each series sharpen as the energy increases, a common feature of Rydberg series.

B. Convergence of collision strengths to Coulomb-Born results

The evaluation of the total cross section in Eq. (20) extends over many partial waves. As discussed above, the high partial waves are amenable to treatment by the Coulomb-Born approximation. We calculate the reactance matrix $\underline{K}^{(\mathrm{CB})}$ by Eq. (23) and from it the collision strength $\Omega^{(\mathrm{CB})L\pi}$ by Eq. (27) for each set $(L\pi)$. In order to show qualitatively the convergence of the Coulomb-Born approximation to the R-matrix with MQDT, Figs. 4–6 display $\Omega^{(\mathrm{CB})L\pi}$ with its counterpart $\frac{1}{2}\sum_S \Omega^{LS\pi}$ for $L \le 7$ for $\mathrm{Be}^+(2s \to 2p)$, $\mathrm{Mg}^+(3s \to 3p)$, and $\mathrm{Ca}^+(4s \to 4p)$. The factor $\frac{1}{2}$ and the summation over S, originating from a comparison of Eqs. (20) and (28), eliminate the spin dependence of the R-matrix results.

The R-matrix and Coulomb-Born results, after notable departures at the partial waves, converge to the values of $\frac{1}{2}\sum_S \Omega^{LS\pi}$ at $L = 7$. This convergence guarantees that the contributions from $L > 7$ are provided adequately by the

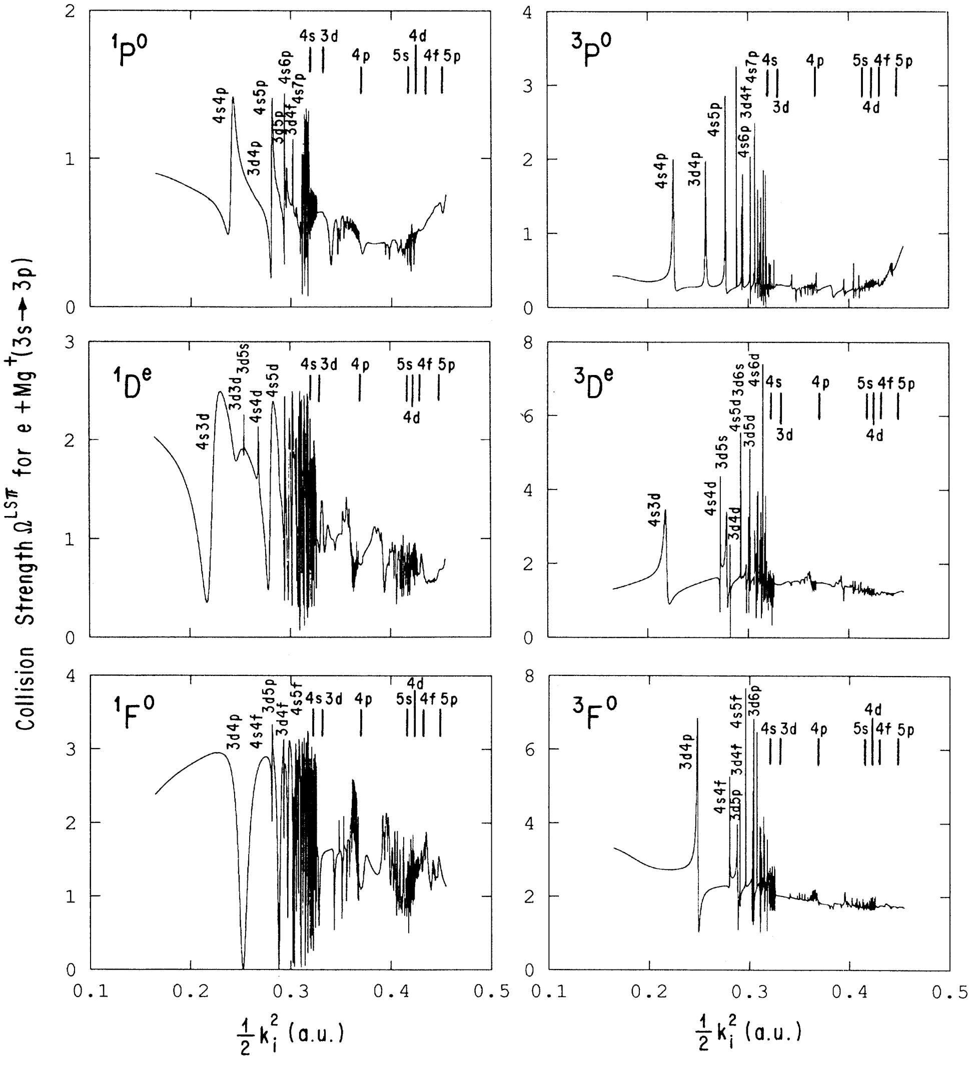

FIG. 2. Same as Fig. 1 for $\mathrm{Mg}^+(3s \to 3p)$.

TABLE I. Double excitation energies (in eV). Energies are relative to the ground states of Be($2s^2$) and Mg($3s^2$).

States ${}^1P^0$	Be Expt.[a]	Present work	States ${}^1P^0$	Mg Expt.[b]	Present work
$3s3p$	17.64	17.64	$4s4p$	14.18	14.17
$3s4p$	18.83	18.84	$4s5p$	15.24	15.23
$3s5p$		19.50	$4s6p$	15.61	15.61
$3s6p$		19.66	$4s7p$	15.83	15.83
$3s7p$	19.81	19.84	$4s8p$	15.98	15.99
$3s8p$	19.91	19.93	$4s9p$	16.06	16.07
$3s9p$	19.99	20.01	$4s10p$	16.11	16.10

[a] References [39] and [40].
[b] References [40] and [41].

Coulomb-Born results. A comparison has also been made by replacing the Coulomb-Born approximation with a plane-wave Born approximation. As expected, the convergence is poor owing to inadequacy of the plane-wave description of the incident electron in the Coulomb field of the target ion.

C. Total inelastic cross section

We have calculated the total inelastic cross sections for the first optical resonance excitations in Be$^+$, Mg$^+$, and Ca$^+$ by summing the collision strengths $\Omega^{LS\pi}$ of the R matrix with MQDT in Eq. (20) up to $L=7$. These cross

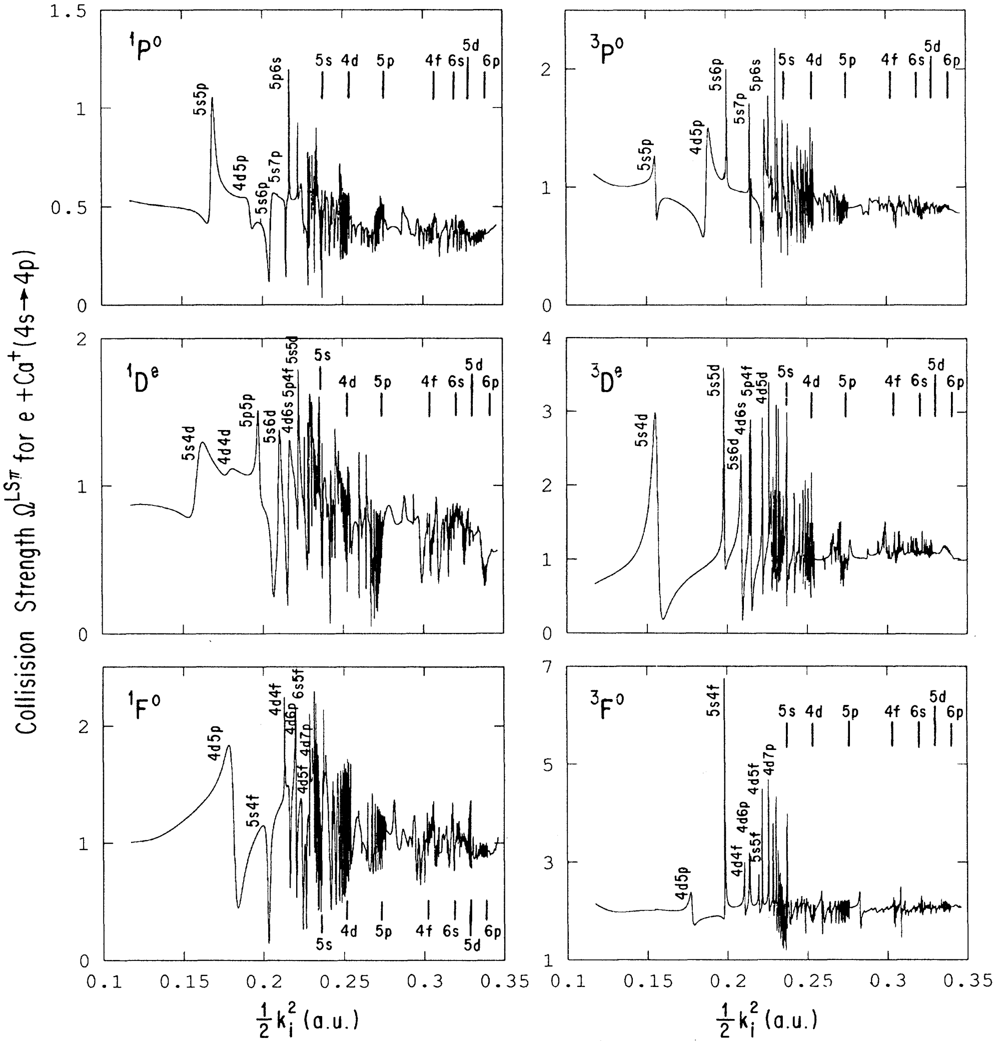

FIG. 3. Same as Fig. 1 for Ca$^+$($4s \rightarrow 4p$).

sections, averaged over a Gaussian of width 0.15 eV, are represented by the curves (a) in Figs. 7–9 together with the experimental photoemission cross sections [11–14,23] indicated by circles with error bars. For these optical excitations of the targets, the high partial waves contribute substantially as the energy increases. Note particularly the rises in the end of the $L=7$ curves in Figs. 4–6. This contribution has been complemented by evaluating $\Omega^{(\mathrm{CB})L\pi}$ for partial waves L up to 20, beyond which they become negligible in our energy range. Cross sections including high-partial-wave contributions are represented by curves (b) in Figs. 7–9. The contributions by partial waves ($L>7$) add only a small fraction at low energy but $\sim 20\%$ to the cross sections by the R matrix with MQDT at high energy.

The cross sections (b) in Figs. 7–9 agree well with the experimental data in the energy range below the thresholds $\{\epsilon^a\}$ of target excitations to higher levels. However, they fall below the experimental fluorescence cross sections above these thresholds. Matching to the experimental data is achieved by adding the contributions of optical cascades from higher levels, as described below, the total being represented by the curves (c).

In the case of $e+\mathrm{Ca}^+$, the emission cross sections $\sigma_{\mathrm{em}}(4p_{3/2}\rightarrow 4s)$ and $\sigma_{\mathrm{em}}(4p_{1/2}\rightarrow 4s)$ have been resolved experimentally [13], yielding the statistical ratio of $\sigma_{\mathrm{em}}(4p_{3/2}\rightarrow 4s)/\sigma_{\mathrm{em}}(4p_{1/2}\rightarrow 4s)\sim 2.0$. Furthermore, a fraction 1/17.6 of the $4p_{3/2}$ excitation [42] decays to the $3d$ metastable state of Ca^+. The observed fluorescence data shown in Fig. 9 pertain to the transition $(4p_{3/2}\rightarrow 4s)$ and are compared with the excitation cross sections $(4s\rightarrow 4p)$ multiplied by the factor [16]

$$\chi=\left[\frac{2}{2+1}\right]\left[\frac{17.6}{17.6+1}\right]=0.6308\ . \tag{29}$$

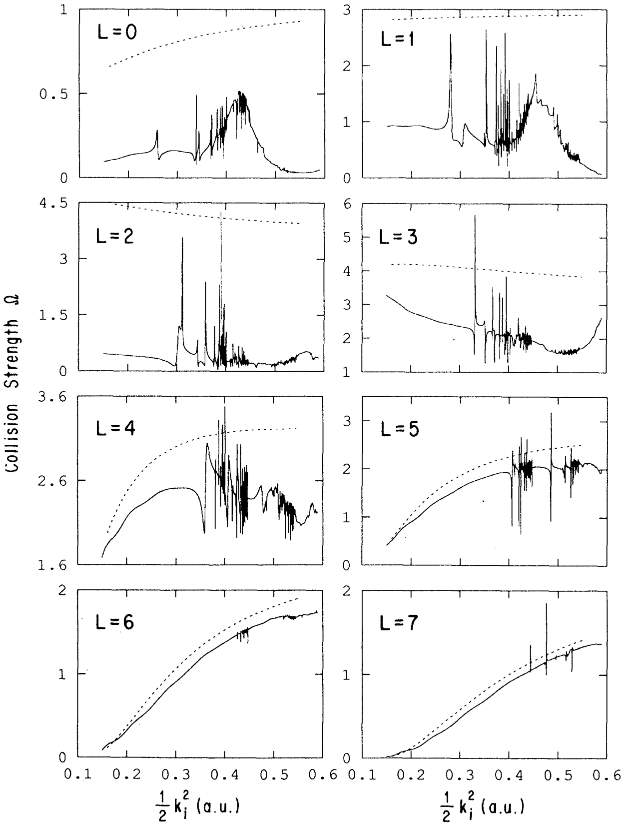

FIG. 4. Dimensionless Coulomb-Born collision strengths $\Omega^{(\mathrm{CB})L\pi}$ (dashed lines) and $\frac{1}{2}\sum_S \Omega^{LS\pi}$ (solid lines) from the R matrix with MQDT for $\mathrm{Be}^+(2s\rightarrow 2p)$. Note the discrepancies at low L and the convergence of $\Omega^{(\mathrm{CB})L\pi}$ to $\frac{1}{2}\sum_S \Omega^{LS\pi}$ at $L=7$.

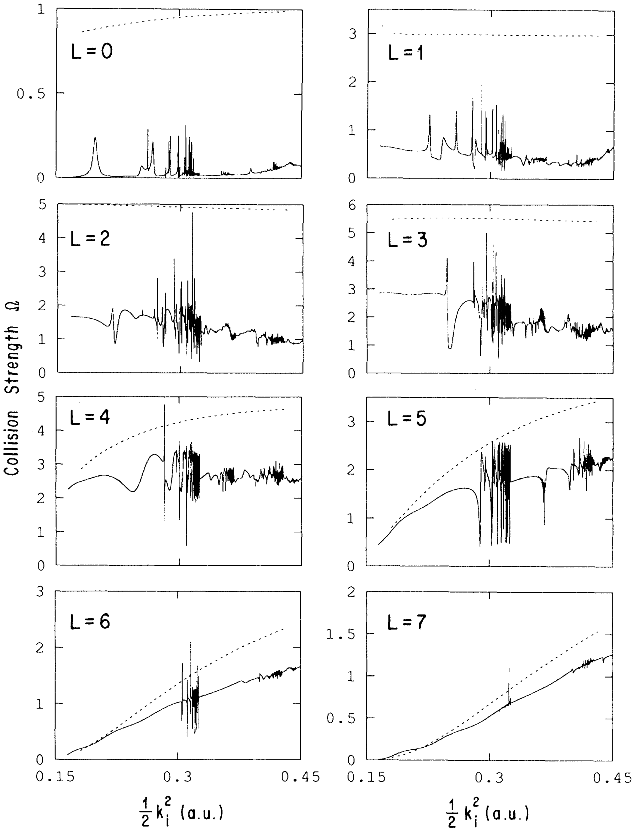

FIG. 5. Same as Fig. 4 for $\mathrm{Mg}^+(3s\rightarrow 3p)$.

D. Excitations to higher levels and cascade effects

As mentioned in Sec. I, the calculated R matrices of each set $(LS\pi)$ contain cross-section information for *all transitions* between target states accessible in our energy range. We have extracted such cross sections for several optically forbidden and allowed excitations of targets, specifically $\sigma(2s\rightarrow 3s)$ and $\sigma(2s\rightarrow 3d)$ for $e+\mathrm{Be}^+$, $\sigma(3s\rightarrow 3d)$ and $\sigma(3s\rightarrow 4s)$ for $e+\mathrm{Mg}^+$, and $\sigma(4s\rightarrow 5s)$, $\sigma(4s\rightarrow 4d)$, and $\sigma(4s\rightarrow 5p)$ for $e+\mathrm{Ca}^+$, all of which contribute to the resonance emission by cascade. These cross sections, ranging from less than one to a few atomic units, are generally much smaller than for the first optical resonance excitation. They also display the prominent resonances due to double excitations of the collision complex. Transitions requiring quadrupole (or higher mul-

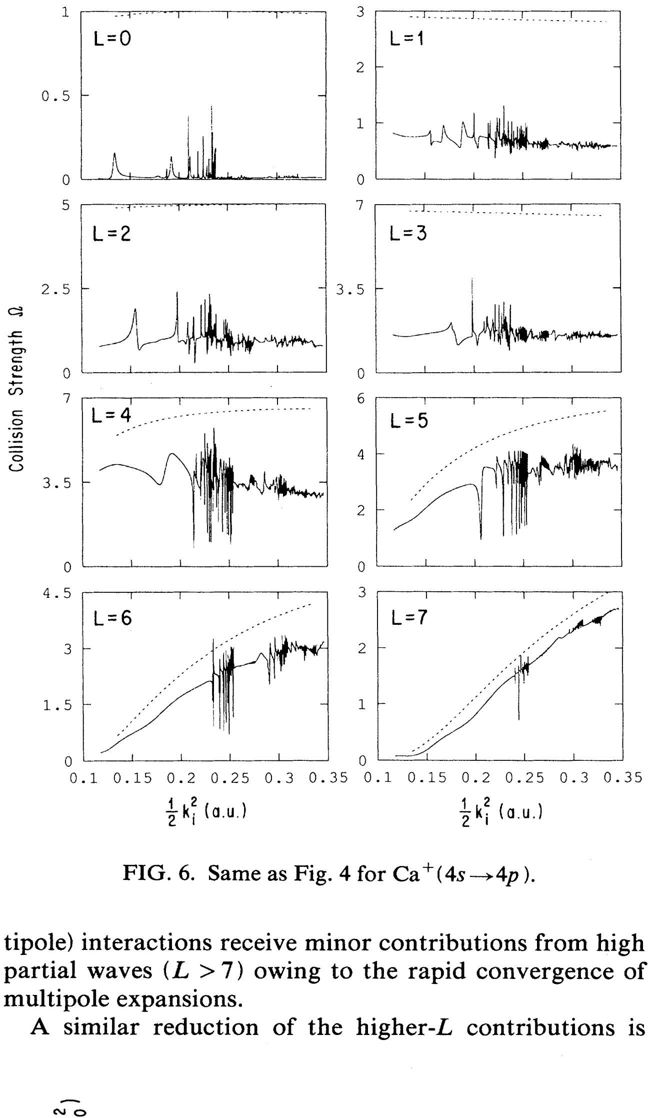

FIG. 6. Same as Fig. 4 for $\mathrm{Ca}^+(4s\rightarrow 4p)$.

tipole) interactions receive minor contributions from high partial waves ($L>7$) owing to the rapid convergence of multipole expansions.

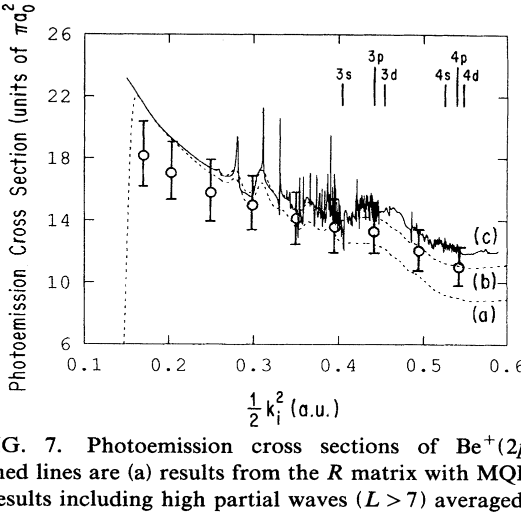

FIG. 7. Photoemission cross sections of $\mathrm{Be}^+(2p\rightarrow 2s)$. Dashed lines are (a) results from the R matrix with MQDT and (b) results including high partial waves ($L>7$) averaged over a Gaussian of width 0.15 eV; the solid line (c) is the result including both high partial waves and cascade effects without Gaussian averages; ○, experimental photoemission cross sections of Ref. [23].

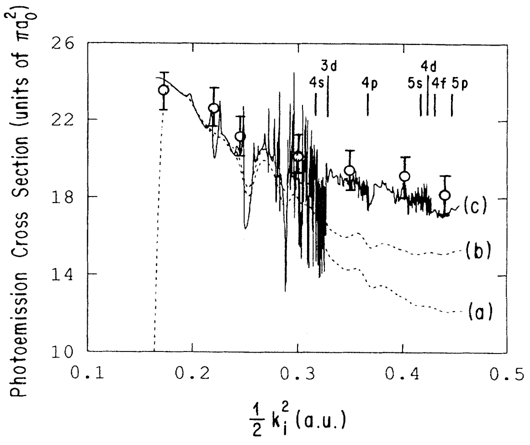

FIG. 8. Same as Fig. 7 for $\mathrm{Mg}^+(3p\rightarrow 3s)$. Experiments from Refs. [11] and [12].

A similar reduction of the higher-L contributions is also noted for dipole transitions to higher-n levels. This reduction stems from the lower residual velocity of the projectile's escape after the collision, as indicated by the low contributions to the cross sections by $\Omega^{LS\pi}$ with $L=6$ and 7. The Coulomb-Born contributions to higher n are similarly negligible for $L>7$.

General propensity rules favor excitations to higher rather than lower angular momenta. Thus we have found, among quadrupole transitions, $\sigma(2s\rightarrow 3d)$ to be larger than $\sigma(2s\rightarrow 3s)$ in $e+\mathrm{Be}^+$. The projectile electron also tends to lose angular momentum, thus reducing the centrifugal barrier to its escape. Excitations within the same shell are also favored, e.g., $\sigma(3s\rightarrow 3d)>\sigma(3s\rightarrow 4s)$ in $e+\mathrm{Mg}^+$ and $\sigma(4s\rightarrow 4d)>\sigma(4s\rightarrow 5s)$ in $e+\mathrm{Ca}^+$.

These cross sections for dipole and quadrupole transitions have served here to evaluate the cascade effects but are not shown for brevity. Figure 10 shows, however, the example $\sigma(4s\rightarrow 3d)$ of $e+\mathrm{Ca}^+$ with its familiar double excitation series.

As noted above, the cross sections for excitation of fluorescence, mainly from the lowest optical resonance

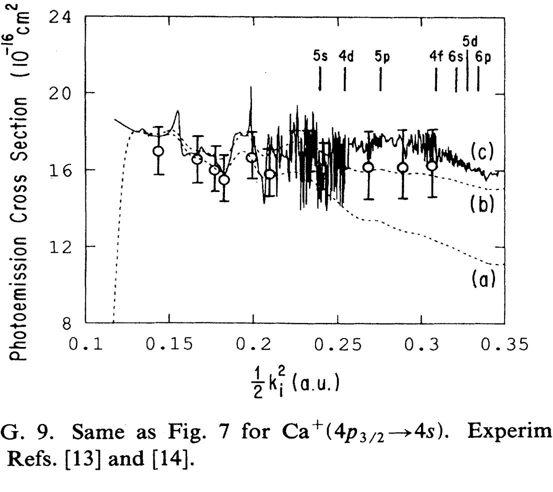

FIG. 9. Same as Fig. 7 for $\mathrm{Ca}^+(4p_{3/2}\rightarrow 4s)$. Experiments from Refs. [13] and [14].

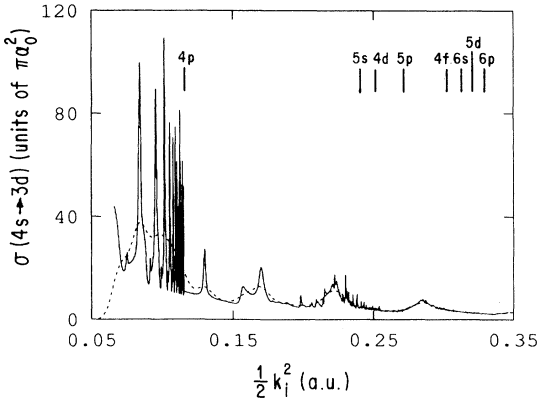

FIG. 10. Total cross section of $Ca^+(4s \rightarrow 3d)$. The dashed line is a Gaussian convolution of the solid line with an energy width 0.15 eV.

level such as $Ca^+(4p)$, include cascade contributions from the excitation to higher accessible levels followed by emission of one or more unobserved photons. In the example of fluorescence from $Ca^+(4p_{3/2})$, we have [16]

$$\sigma_{em}(4p_{3/2} \rightarrow 4s) = \chi[\sigma(4s \rightarrow 4p) + \sigma(4s \rightarrow 5s) + \sigma(4s \rightarrow 4d) + 0.91\sigma(4s \rightarrow 5p)] \; . \tag{30}$$

The coefficient χ of Eq. (30) represents the fraction of transitions to $4p$ in its fine-structure component $4p_{3/2}$. In this example, the $5s$ and $4d$ level decay to $4p$ directly by dipole emission, whereas the $5p$ state decays through two consecutive transitions, via $5s$ or $4d$. The additional 0.91 coefficient in (30) represents the probability, evaluated in Ref. [16], that the $5p$ level does not decay to $4s$ and $3d$ directly; the contribution to (30) from additional cascade paths appears negligible.

Curves (c) in Figs. 7–9 represent the calculated photoemission cross sections after including the cascade effects for Be^+, Mg^+, and Ca^+, which have significantly improved the agreement between our results and experimental data.

E. Differential cross sections

Cross sections differential in the scattering angle for $Be^+(2s \rightarrow 2p)$, $Mg^+(3s \rightarrow 3p)$, and $Ca^+(4s \rightarrow 4p)$ have been evaluated by Eq. (21) with the calculated $\underline{T}$ matrix elements. We are particularly interested in the different manifestations of collisions near their double excitation resonances. We have displayed these differential cross sections in three dimensions in Fig. 11, only for $e + Ca^+$ for brevity. The vertical axis represents the value of the differential cross section and the two horizontal axes are for the scattering angle θ and the incident energy $\frac{1}{2}k_i^2$. The double excitation resonances appear on the surface as bumps which become generally more prominent near the forward- and backward-scattering angles but are less visible in the intermediate range of θ [Fig. 11(b)]. Another interesting phenomenon, displayed in Fig. 11(a), is that backward scattering actually dominates forward scattering near the excitation threshold. However, the differential cross section gradually tends toward forward scattering in the collision as the incident energy $\frac{1}{2}k_i^2$ increases [Fig. 11(b)]. Lengyel *et al.* [17] have also calculated some differential cross sections for $Be^+(2s \rightarrow 2p)$ and $Mg^+(3s \rightarrow 3p)$ that agree reasonably with ours. We are not aware of relevant experimental data and hope that these initial results will stimulate further efforts.

F. Polarization of emitted photons

The percentage P of linear polarization for the $2p \rightarrow 2s$ emission in Be^+ and the $4p_{3/2} \rightarrow 4s$ in Ca^+ have been measured experimentally [13,14,23]. Seaton *et al.*

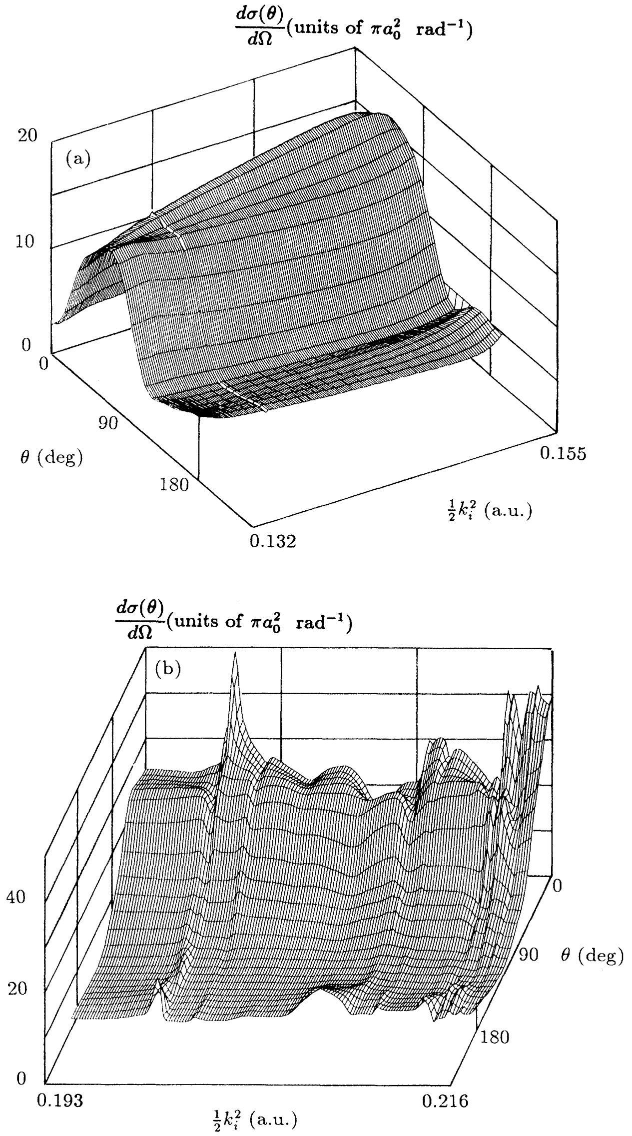

FIG. 11. Differential cross sections for $Ca^+(4s \rightarrow 4p)$ in different energy ranges.

[43,44] have determined P in terms of the partial cross section $\sigma_{M_{L_f}}(i \rightarrow f)$ of Eq. (22) for excitation to Zeeman levels M_{L_f},

$$P = \frac{300(9\gamma - 2)(\sigma_0 - \sigma_1)}{12\sigma_0 + 24\sigma_1 + (9\gamma - 2)(\sigma_0 - \sigma_1)} \tag{31}$$

for $\mathrm{Be}^+(2p \rightarrow 2s)$ and

$$P = \frac{300(\sigma_0 - \sigma_1)}{5\sigma_0 + 7\sigma_1} \tag{32}$$

for $\mathrm{Ca}^+(4p_{3/2} \rightarrow 4s)$, respectively.

The parameter γ in (31) depends on the hyperfine splittings of Be^+, as discussed by Mitroy and Norcross [27]. Figure 12 represents the calculated polarization P together with the experimental data for $\mathrm{Be}^+(2p \rightarrow 2s)$ and $\mathrm{Ca}^+(4p_{3/2} \rightarrow 4s)$ using $\gamma = 0.44$ as in Ref. [27]. The dashed curves (a), evaluated with the partial waves $(L \leq 7)$ from the R matrix with MQDT and averaged over a Gaussian of width 0.15 eV, agree well with the experimental data at low energy but deviate at high energy. Inclusion of the high partial wave contributions by the Coulomb-Born approximation, in the solid curves, eliminates these deviations.

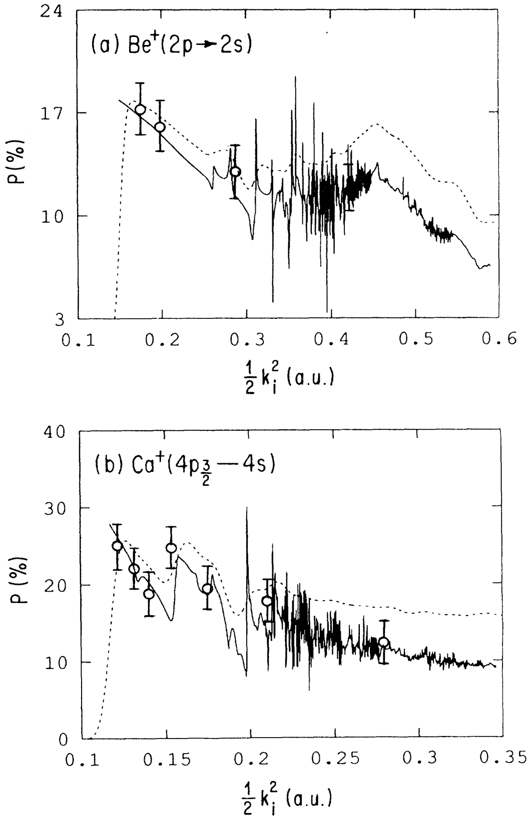

FIG. 12. Polarizations of emitted photons from (a) $\mathrm{Be}^+(2p \rightarrow 2s)$ and (b) $\mathrm{Ca}^+(4p_{3/2} \rightarrow 4s)$. Dashed lines represent the R matrix with MQDT calculations averaged over a Gaussian of width 0.15 eV; solid lines include contributions from high partial waves $(L > 7)$; ○, experimental results of Ref. [23] for $\mathrm{Be}^+(2p \rightarrow 2s)$ and Refs. [13] and [14] for $\mathrm{Ca}^+(4p_{3/2} \rightarrow 4s)$.

IV. DISCUSSION

The present study has demonstrated a noteworthy application of the eigenchannel R-matrix treatment of electron-ion collisions. This treatment of collisions with short impact parameter, specifically with $L \leq 7$, yields good cross sections and reveals details of the double excitation resonances. Its results are then combined with the appreciable contribution of large impact parameters evaluated by the Coulomb-Born approximation. Our results agree well with experimental results. Specifically, the calculated cross section of $\mathrm{Be}^+(2p \rightarrow 2s)$ has been brought into closer agreement with the experimental data shown in Ref. [23] than had been achieved previously, predicting numerous resonances that have not yet been resolved experimentally. Agreement has also been obtained for $\mathrm{Mg}^+(3p \rightarrow 3s)$ and $\mathrm{Ca}^+(4p_{3/2} \rightarrow 4s)$, with prediction of similar double excitation series.

A. Comparison with previous treatments

Many calculations on electron-ion collisions have been done by Coulomb-Born approximation, the distorted-wave approximation, close coupling, the diagonalization method, and other procedure [18,19,45]. Coulomb-Born distorted-wave approximation [45–49] give cross sections generally higher than experimental results and hardly any resonances, through disregarding the strong correlations between the projectile and target electrons.

The most advanced close-coupling calculation for $e + \mathrm{Be}^+(2s \rightarrow 2p)$ has been made in Ref. [27]. These cross sections are closer to the experimental data than any earlier results, but still do not fall within the experimental error bars. No evidence of double excitation resonances appears in this reference, but some evidence appears in the parallel calculation [16] for $e + \mathrm{Ca}^+(4s \rightarrow 4p)$. This Ca^+ calculation gives reasonable agreement with experimental cross sections.

Lengyel *et al.* [17] have evaluated the cross sections for $e + \mathrm{Be}^+(2s \rightarrow 2p)$ and $e + \mathrm{Mg}^+(3s \rightarrow 3p)$ by a diagonalization method that utilizes a basis set including some double excitation states of the complex, constructed by a configuration-interaction method. Inclusion of such states causes the corresponding resonances to appear. The resulting cross sections for $e + \mathrm{Be}^+(2s \rightarrow 2p)$ are more than ~20% higher than the experimental data but those for $e + \mathrm{Mg}^+(3s \rightarrow 3p)$ agree better with the experimental measurements.

We have complemented here the scarce evidence of resonant series in previous calculations by utilizing the full reactance matrix $\underline{K}^o$ of Eq. (16). The present calculation contrasts those discussed above by proceeding throughout the volume V without any reference to the fragmentation channels external to V, thus acquiring greater flexibility and efficiency.

B. Prospective extensions

Extension of the present work to collisions with heavier alkaline-earth-metal ions would require explicit treatment of the fine structure of target excitations. This structure, disregarded here even though appreciable in Ca^+ experiments, requires a transformation from LS to jj coupling previously implemented in spectroscopy studies [6,22]. Polarization of the target ion at long range should also be treated [9].

Parallel calculations along the isoelectronic sequences of alkaline-earth-metal ions would reflect the increasing influence of the ionic charge. Extension to ions with multielectron open shells hinges on the recent development of the corresponding calculation of neutral spectra [50].

The mapping of radial correlations [7,29], important for understanding both the correlation mechanism and the resulting channel interactions, remains to be investigated systematically in the present application.

Extension to electron collision with neutral atoms is, of course, of greater interest but will require the construction of different orbitals for the negative-ion complex in its various excited states. This extension is accessible through the R matrix for the negative-ion complex with replacement of the Coulombic wave functions $\{f,g\}$ by wave functions for the field of a neutral but polarizable target atom [51,52].

C. Accuracy limits from truncations

Practical limits to computational effort impose a limit to the accuracy of results. This limit has emerged specifically from the selection of a modest set of channels in close-coupling treatments. In the present treatment, too, the selection of channels has set a lower limit to the radius r_0 of the R-matrix volume V.

Within this volume the selection of a finite set of orbitals renders the basis set incomplete. Its adequacy has been tested through the convergence of results with increasing the number of orbitals, but a qualitative change of orbitals might conceivably have proved otherwise.

In the analogous problems of energy-level calculations, the *monotonic* decrease of theoretical estimates with increasing basis provides a dependable guidance. A corresponding guidance is afforded in the calculation of eigenchannel phases which are necessarily lower than their actual values. Cross-section values, however, depend generally on the contribution of many eigenchannels. Accordingly it is generally difficult to derive guidance from the trend of collision parameters with increasing effort, even though it has been argued occasionally that excluding a wave function from a portion of configuration space would boost a cross section artificially [53].

In the present treatment a restriction has been imposed by barring both electrons from trespassing the surface S simultaneously. This limit would be removed when adequate two- (or more-) electron wave functions become available for the ion's long-range field.

The dependence of the radius r_0 on the total energy E, described in Sec. II, might suggest that the R-matrix volume V would necessarily diverge with increasing energy. This conclusion, however, is unwarranted because significant correlations among electrons of eV energy are necessarily confined to a finite volume. Exploration of this circumstance in the study of higher-energy collisions remains undeveloped.

ACKNOWLEDGMENTS

I would like to express my deep gratitude to Professor U. Fano for his continual guidance and support throughout this work and for his assistance with the manuscript. I am also indebted to Professor C. H. Greene for sharing his expertise and providing the streamlined R-matrix code together with insightful advice. This work was supported by National Science Foundation Grants Nos. PHY86-10029 and 89-18304.

---

[1] X. C. Pan and U. Fano, Phys. Rev. A **39**, 4502 (1989); U. Fano and M. Inokuti, Argonne National Laboratory Report No. ANL-76-80 (1976) (unpublished).

[2] X. C. Pan and A. Chakravorty, Phys. Rev. A **41**, 5962 (1990).

[3] X. C. Pan, Phys. Rev. Lett. **66**, 2972 (1991).

[4] U. Fano and C. M. Lee, Phys. Rev. Lett. **31**, 1573 (1973).

[5] M. J. Seaton, Rep. Prog. Phys. **46**, 97 (1983), and references therein.

[6] C. M. Lee and K. T. Lu, Phys. Rev. A **8**, 1241 (1973).

[7] P. F. O'Mahony and C. H. Greene, Phys. Rev. A **31**, 250 (1985), M. Aymar, J. Phys. B **20**, 6507 (1987).

[8] Longhuan Kim and C. H. Greene, Phys. Rev. A **38**, 2361 (1988).

[9] C. H. Greene and M. Aymar, Phys. Rev. A **44**, 1773 (1991).

[10] C. H. Greene, Phys. Rev. A **42**, 1405 (1990).

[11] I. P. Zapesochny, A. I. Imre, V. I. Frontov, A. N. Gomonay, and A. I. Dashchenko, in *Proceedings of the 8th International Conference on Physics of Electronic and Atomic Collisions, Berlin,* edited by J. Eichler, W. Fritsch, I. V. Hertel, N. Stolterfoht, and U. Wille (North-Holland, Amsterdam, 1983), p. 751.

[12] V. A. Kel'man, A. I. Dashchenko, I. P. Zapesochny, and A. I. Imre, Dokl. Acad. Sci. (USSR), **220**, 65 (1975).

[13] P. O. Taylor and G. H. Dunn, Phys. Rev. A **8**, 2304 (1973).

[14] I. P. Zapesochny, V. A. Kel'man, I. A. Imre, A. I. Dashchenko, and F. F. Danch, Zh. Eksp. Teor. Fiz. **69**, 1948 (1975) [Sov. Phys.—JETP **42**, 989 (1976)].

[15] C. Mendoza, J. Phys. B **14**, 2465 (1981).

[16] J. Mitroy, D. C. Griffin, and D. W. Norcross, Phys. Rev. A **38**, 3339 (1988).

[17] V. I. Lengyel, V. T. Navrotsky, and E. P. Sabad, J. Phys. B **23**, 2847 (1990).

[18] P. G. Burke W. D. Robb, *Advances in Atomic and Molecular Physics,* edited by D. R. Bates and B. Bederson (Academic, New York, 1975), Vol. 11, p. 144.

[19] P. G. Burke, *Atomic Physics,* edited by H. Narumi and I. Shimamura (North-Holland, Amsterdam, 1987), Vol. 10, p. 243.

[20] A. Burgess, D. G. Hummer, and J. A. Tully, Philos. Trans. A **266**, 225 (1970).

[21] U. Fano and J. H. Macek, Rev. Mod. Phys. **45**, 553 (1973).

[22] Longhuan Kim and C. H. Greene, Phys. Rev. A **36**, 4272 (1987).

[23] P. O. Taylor, R. A. Phaneuf, and G. H. Dunn, Phys. Rev. A **22**, 453 (1980).

[24] E. P. Wigner and L. Eisenbud, Phys. Rev. **72**, 29 (1947).

[25] C. H. Greene, Phys. Rev. A **28**, 2209 (1983); **32**, 1880 (1985); J. Opt. Soc. Am. B **4**, 775 (1987).

[26] H. Le. Rouzo and G. Raseev, Phys. Rev. A **29**, 1214 (1984).

[27] J. Mitroy and D. W. Norcross, Phys. Rev. A **37**, 3755 (1988).

[28] C. H. Greene and Longhuan Kim, Phys. Rev. A **38**, 5953 (1988).

[29] C. H. Greene and Longhuan Kim, Phys. Rev. A **36**, 2706 (1987).

[30] D. W. Norcross and M. J. Seaton, J. Phys. B **9**, 2983 (1976).

[31] C. E. Moore, *Atomic Energy Levels,* Natl. Bur. Stand. (U.S.) Circ. No. 467 (U.S. GPO, Washington, DC, 1971).

[32] U. Fano and A. R. P. Rau, *Atomic Collisions and Spectra* (Academic, Orlando, 1986).

[33] J. M. Blatt and L. C. Biedenharn, Rev. Mod. Phys. **24**, 258 (1952).

[34] K. Smith, *Calculation of Atomic Collision Processes* (Wiley-Interscience, New York, 1971).

[35] M. Rotenberg, R. Bivins, N. Metropolis, and J. K. Wooten, Jr., *The 3j and 6j Symbols* (Technology, MIT, Cambridge, 1959).

[36] H. van Regemorter, Mon. Not. R. Astron. Soc. **121**, 213 (1960).

[37] A. Burgess and V. B. Sheorey, J. Phys. B **7**, 2403 (1974).

[38] A. R. Edmonds, *Angular Momentum in Quantum Mechanics* (Princeton University Press, Princeton, 1974), p. 114.

[39] J. M. Esteva, G. Mehlman-Ballofet, and J. Romand, J. Quantum Spectrosc. Radiat. Trans. **12**, 1291 (1972).

[40] G. Mehlman-Ballofet and J. M. Esteva, Astrophys. J. **157**, 945 (1969).

[41] M. A. Baig and J. P. Connerade, Proc. R. Soc. London Ser. A **364**, 353 (1978).

[42] A. C. Gallagher, Phys. Rev. **157**, 24 (1967).

[43] D. R. Flower and M. J. Seaton, Proc. Phys. Soc. London **91**, 59 (1967).

[44] I. C. Percival and M. J.Seaton, Philos. Trans. R. Soc. London A **251**, 113 (1958).

[45] K. L. Baluja, P. G. Burke, and A. E. Kingston, J. Phys. B **13**, L543 (1980).

[46] M. A. Hayes, D. W. Norcross, J. B. Mann, and W. D. Robb, J. Phys. B **10**, L429 (1977).

[47] M. Blaha, Astron. Astrophys. **16**, 437 (1972).

[48] M. Chidichimo, J. Phys. B **14**, 4149 (1981).

[49] J. V. Kennedy, V. P. Myerscough, and M. R. C. McDowell, J. Phys. B **11**, 1303 (1978).

[50] F. Robicheaux (private communication).

[51] S. Watanabe and C. H. Greene, Phys. Rev. A **22**, 158 (1980).

[52] S. Watanabe, Phys. Rev. A **25**, 2074 (1982).

[53] U. Fano, Comments At. Mol. Phys. **1**, 159 (1970).